

## Transport barrier dynamics

W. Horton and P. Zhu

*Institute for Fusion Studies, The University of Texas, Austin, Texas 78712*

(Received 27 January 2000; accepted 17 July 2000)

The properties of the internal transport barriers are developed using theory and radial transport simulations that evolve local turbulent energy density with the temperature profiles. Standard ion temperature gradient models for the nonlinear radial fluxes driven by drift wave turbulence and stabilized by flow shear are implemented in a new high resolution multiple space–time transport code. A dimensionless parameterization of the input power is introduced and shown to characterize the bifurcation to an internal transport barrier. Examples of the interaction and feedback loops of the turbulence with the transport profiles are given for transport barriers as in the Tokamak Fusion Test Reactor [D. J. Grove *et al.* Nucl. Fusion **25**, 1167 (1985)] and the Japan Atomic Energy Research Institute Tokamak-60 Upgrade (JT-60U) [Ninomiya *et al.*, Phys. Fluids B **4**, 2070 (1992)]. For the JT-60U the high performance discharge E 27969, which reached an equivalent  $Q_{DT}$  of unity, is modeled with an appropriate set of turbulent thermal, angular momentum and particle diffusivities. The bifurcation analysis suggests a scaling law for the critical power for the onset of internal transport barriers. © 2000 American Institute of Physics. [S1070-664X(00)00411-0]

### I. INTRODUCTION

The formation of significant internal transport barriers in the large ( $I > 1$  MA) tokamak confinement experiments is of fundamental importance to the science of plasma confinement and to the achievement of controlled fusion power. The internal transport barrier (ITB) is now produced in all major tokamaks.<sup>1,2</sup> The strongest transport barriers are associated with reversed magnetic shear and  $E_r$ -shear while weaker barriers are associated primarily with one or the other mechanism.<sup>3,4</sup> The transport barrier formation process appears to require a true bifurcation of the radial flux as a function of the driving gradients. Bifurcations are typical in driven-dissipative systems with a large number of interacting subcomponents.

In the steady state the injected particles, energy and momentum flow through the tokamak system by the transport processes with its many subcomponents and then exit through the scrape-off layer (SOL) into the divertor chamber. Power and momentum flow into the system and drive up the gradients of the even-velocity fluid moments (density and pressure) and the odd-velocity fluid moments (flow velocity and thermal flux), respectively. The drift wave turbulent energy density  $W(r, t)$  responds in a complex manner on a fast time scale. There are growth terms from the temperature gradients, damping terms from the current-driven magnetic shear and the flow-driven  $E_r$ -shear; and there is the nonlinear mode coupling transfer of turbulence energy to spectral regions of strong wave damping along with wave propagation. In addition there are the transport processes due to the Coulomb collisions given by the neoclassical theory. Clearly, there are multiple feedback and feedforward loops in the system. As the system parameters change, there will be abrupt changes in the pathways taken by the flow of energy and momentum through the subcomponents to the scrape-off layer plasma connected to the divertor chamber and to the

walls of the device. These changes are the bifurcations that have been traditionally studied in simpler settings such as a few coupled partial differential equations or their projection onto low-order ordinary differential equation systems.<sup>5–7</sup> The simplest model of the bifurcation from the turbulence and shear mass flow is described by Diamond *et al.*<sup>8</sup> as the predator–prey model with two ordinary differential equations. How many degrees of freedom are required to describe the system is unknown and, of course, depends on the level of detail sought in the description. The Diamond group models are developed in more detail in Lebedev and Diamond<sup>9</sup> and Newman *et al.*<sup>10</sup>

Local microscopic theories of plasma turbulence give one bifurcation mechanism through a symmetry breaking of the temperature gradient driven convective vortices that results in the onset of sheared  $\mathbf{E} \times \mathbf{B}$  flows.<sup>11</sup> Computer simulations of both fluid equations<sup>5–7,12</sup> show the Reynolds stress driven onset of sheared flows. The energy conservation of the system<sup>13</sup> works to show that the energy created in the shear zonal flows shows up as the shear flow damping term in the linear growth rate. Here we do not dwell on these well-known aspects of the microscopic processes but rather investigate the global transport properties associated with the bifurcations.

A challenging part of the transport barrier dynamics (TBD) problem is the necessity to describe the fast formation of steep radial gradients in the transport code. To meet this challenge we have developed a new high resolution transport code called TBD for the CRAY T3E using message passing interface (MPI) and FORTRAN 90 (NERSC, 1998 Annual Report, p. 88). The code has been run with four thermodynamic transport fields with up to  $N_x = 1000$  radial grid points and through  $N_t = 10^6$  time steps. The radial zones are distributed over the processing elements. The time advancement is through the adaptive Runge–Kutta 5th–6th order initial value integrator known as DVERK.<sup>14</sup> This integrator is

loaded into each processor to reduce message passing between the processors.

By using this high-order time integration, the fast-growing gradients over mesoscale lengths (the geometric mean of the gyroradius scale and the mirror radius  $a$  of the system) produced by the bifurcations are accurately followed.

In Sec. II we review the general structure of the transport equations for toroidally rotating plasma. In Sec. III we give the equations used to compute the turbulent energy density and the  $E_r$ -shearing, and present several examples of transport barrier models. The simulation results of the transport models are given and discussed in Sec. IV. In Sec. V we derive two scaling laws for the power required for ITB formation. Finally, the conclusions are given in Sec. VI.

## II. STRUCTURE OF THE TRANSPORT EQUATIONS

The general form of the coupled particle, thermal energy, and toroidal momentum transport equations is derived in Sugama and Horton.<sup>15</sup> In axisymmetric systems, the magnetic field  $\mathbf{B} = I\nabla\zeta + \nabla\zeta \times \nabla\Psi$  and the toroidal rotation velocity  $V_t = R\nabla\zeta = -Rcd\Phi/d\Psi$  in magnetic flux coordinates. Here  $\zeta$  is the toroidal angle,  $\Psi$  represents the poloidal flux,  $I = RB_T$ , and the angular velocity of toroidal rotation is the contravariant velocity component  $V^\zeta = V_t/R$ , where  $V_t$  is the linear toroidal velocity. The particle species is designated by the subscript  $a$ , and the surface fluid velocity is  $\mathbf{u}_a = \mathbf{V}_t + \mathbf{u}_{a1}$  with the toroidal velocity  $\mathbf{V}_t$  common to all species. In the equations below, the flux surface average is defined as

$$\langle F \rangle = \frac{1}{V'} \int_0^{2\pi} \frac{d\theta}{B^\theta} F(\Psi, \theta), \quad (1)$$

where

$$V' = \int_0^{2\pi} \frac{d\theta}{B^\theta} = \int_0^{2\pi} \frac{d\theta}{\nabla\Psi \cdot \nabla\theta \times \nabla\zeta}, \quad (2)$$

and  $\theta$  is the poloidal angle. The particle transport equation is

$$\frac{\partial n_a}{\partial t} + \frac{1}{V'} \frac{\partial}{\partial\Psi} (V' \Gamma_a) = S_a^{\text{in}} - S_a^{\text{out}}, \quad (3)$$

and the thermal balance equation is

$$\begin{aligned} & \frac{\partial}{\partial t} \left\langle \left( \frac{3}{2} p_a + n_a e_a \tilde{\Phi}_1 \right) \right\rangle + \frac{1}{V'} \frac{\partial}{\partial\Psi} \left[ V' \left( q_a + \frac{5}{2} T_a \Gamma_a \right) \right] \\ & = -\Pi_a \frac{\partial V^\zeta}{\partial\Psi} - e_a \Gamma_a \frac{\partial \langle \Phi_1 \rangle}{\partial\Psi} + \langle e_a n_a \mathbf{u}_{a1} \cdot \mathbf{E}^{(A)} \rangle \\ & + \left\langle e_a n_a \frac{\partial \tilde{\Phi}_1}{\partial t} \right\rangle + \frac{1}{2} (V^\zeta)^2 \frac{\partial}{\partial t} \langle m_a n_a R^2 \rangle + P_a - p_a^{\text{out}}, \end{aligned} \quad (4)$$

where  $p_a = n_a T_a$  is the pressure,  $q_a$  is the surface averaged radial heat flux,  $\Pi_a$  is the surface-averaged radial flux of toroidal angular momentum and  $\mathbf{E}^{(A)} = -\partial\mathbf{A}/c\partial t$  is the inductive electric field. The fluxes  $\Gamma_a, q_a$  are the usual contravariant components of the physical vectors  $\mathbf{\Gamma}_a, q_a$  given by  $\Gamma_a = \langle \nabla\Psi \cdot \mathbf{\Gamma}_a \rangle (\approx RB_p \Gamma_{ra})$  and  $q_a = \langle \nabla\Psi \cdot q_a \rangle (\approx RB_p q_{ra})$  in

the small aspect ratio limit. The first order flow velocities  $\mathbf{u}_{a1}$  in Eq. (3) are incompressible with the perpendicular components driven by

$$\mathbf{u}_{\perp a1} = \frac{c}{e_a B^2} \mathbf{B} \times \left( \frac{1}{n_a} \nabla p_a + e_a \nabla \Phi_1 - m_a (V^\zeta)^2 R \nabla R \right). \quad (5)$$

The term  $-e_a \Gamma_a \partial \langle \Phi_1 \rangle / \partial\Psi$  on the right-hand side of Eq. (4) contains an anomalous energy exchange due to the fluctuation induced particle transport  $I_a$ . It has been shown that this anomalous energy exchange rate term is independent of the first order radial electric field. When  $V_t \ll V_i$  or  $r/R \ll 1$  the terms associated with  $\tilde{\Phi}_1$  in Eq. (3) are ignorable since  $e\Phi/T_i = \mathcal{O}[(r/R)(V_t/V_i)^2]$  when  $V_i = (T_i/m_i)^{1/2}$ .

The angular momentum transport equation is only simple when summed over all species

$$\begin{aligned} & \frac{\partial}{\partial t} \left\langle \left( \sum_a m_a n_a \right) R^2 V^\zeta \right\rangle + \frac{1}{V'} \frac{\partial}{\partial\Psi} \left( V' \sum_a \Pi_a \right) \\ & = \mathcal{T}_{\text{in}} - \tau_{\text{out}}. \end{aligned} \quad (6)$$

The torque input is

$$\mathcal{T}_{\text{in}} = \left\langle \sum_a \int d^3v m_a R \hat{\zeta} \cdot \mathbf{V} C_a \right\rangle, \quad (7)$$

where  $C_a$  is the effective collision operator— $\delta f_a / \delta t$  describing the auxiliary input from external sources. The summation over species is used to cancel the exchange in momentum between species  $a$  and  $b$ .

The transport system formed by Eqs. (3)–(7) is closed by transport relations linking the radial fluxes and the radial gradients. The transport coefficients are the summations of both (neo)classical and turbulent contributions, while the later is dominant for most cases. The turbulent transport coefficients depend on the turbulence level, which are determined by the turbulence evolution equation.<sup>15</sup> The complete system of transport equations for density, temperature, toroidal momentum, and turbulence amplitude, are further reduced to various transport model equations after proper approximations. In the next section, we will discuss such models that simulate the internal transport barriers in toroidal confinement systems.

## III. TRANSPORT MODELS FOR TRANSPORT BARRIERS

### A. Turbulent energy density evolution

The turbulence producing the anomalous transport evolves according to the linear growth rate  $\gamma'$  including the effect of the sheared mass flows and the nonlinear saturation from mode coupling. The time scale for the balance between the growth and nonlinear saturation is very short compared to transport time scale  $\tau_L$  so that  $\gamma' \tau_L \sim (L_T/\rho_s)^2 \sim 10^4$ . The exception occurs at the points of marginal stability where  $\gamma' \sim 0$ . Two methods are available for dealing with these disparate time scales. The first numerical method, called subcycling, is to integrate numerically the equation  $dW/dt$  for the turbulence between each time step of the whole set of transport equations. Here,  $W(r, t)$  is the turbulence energy den-

sity. This is a powerful, but computationally intensive, method for dealing with the multitime scale problem of the coupled evolution of the turbulence energy density, density, temperature, and toroidal momentum profiles. The second method is to reduce the  $W(r, t)$  equations sufficiently to allow analytic representations for their evolution between each transport time step. This is the method we develop here re-serving the subcycloning method for a future work.

The time scale for the drift wave growth rate is traditionally taken as  $L_T/c_s$  in the literature, where  $L_T = -(d \ln T/dr)^{-1}$  and  $c_s = (T_e/m_i)^{1/2}$ . For transport codes with evolving profiles, however, a more straightforward choice is  $R/c_s(T_e^0)$  where  $R$  is the fixed major radius of the device and  $T_e^0$  is a reference electron temperature such as 1 keV. The ratio of the time scales is then

$$\gamma_0 = \frac{\tau_L c_s}{R} = \left(\frac{a}{\rho_s}\right)^2 \frac{a}{R}, \quad (8)$$

where we use  $\tau_L = a^2/\chi_{gB}$  with  $\chi_{gB} = \rho_s^2 c_s/a$  in obtaining Eq. (8). Here  $\chi_{gB}$  is the small scale gyro-Bohm drift wave diffusivity. For a Bohm-L mode<sup>16,17</sup> scaling  $\tau_L = a^2/\chi_B$  with  $\chi_B = \rho_s c_s$  the scaling of  $\gamma_0$  increases linearly with  $a/\rho_s$ . The growth rate for the ion temperature gradient (ITG) turbulence with  $\mathbf{E} \times \mathbf{B}$  flow is approximately

$$\gamma^l = \frac{c_s}{R} \left[ \frac{R}{L_{T_i}} - \left( \frac{R}{L_{T_i}} \right)_c - 0.3 Y_s^2 \right] \equiv \frac{\hat{\gamma}^l}{\tau_L} \gamma_0, \quad (9)$$

where the  $\mathbf{E} \times \mathbf{B}$  shear flow parameter  $Y_s$  is given by

$$Y_s = \frac{R}{c_s} \frac{d \ln \Phi}{d \ln q} \approx \frac{L_s}{c_s} \frac{dv_E}{dr} \quad (10)$$

from Horton *et al.*<sup>18</sup> Here  $L_s = qR/s$  with  $s = rq'/q$  is the magnetic shear length. The effect of  $Y_s$  on the transport is explored in 3D simulations in Hamaguchi and Horton.<sup>12</sup> The growth, decay and propagation of the turbulence  $W(r, t)$  in the transport time step  $\Delta t$  is divided into a first step of pure growth and saturation given by

$$\frac{dW}{dt} = 2 \gamma_0 [\hat{\gamma}^l - \hat{\gamma}^{nl} W] W \quad (11)$$

followed by a second step for the propagation with radial group velocity  $v_g = \partial \omega / \partial k_x > 0$  and possibly a small radial diffusivity  $\mu_W$  from the wave dispersion  $\mu_W = \partial^2 \omega / \partial k_x^2 \approx |\omega_*| \rho_s^2$ . Here, the time  $t$  is normalized by  $\tau_L$ . Generally, we take  $\mu_W = 0$  and most studies reported here also take the radial transport with  $v_g = 0$  for radial group velocity of the drift waves. This is the condition appropriate to eigenmodes. There is some evidence from the global three-dimensional (3D) simulations that  $v_g \neq 0$  and so the allowance for  $v_g$  and  $\mu_W$  is incorporated into the calculation of  $W(r, t)$ , as shown later in this section.

The form of the nonlinear restoring force  $\hat{\gamma}^{nl} W = \langle k_x^2 \rangle W$  in Eq. (11) is well known from turbulence theory. What remains unsettled is the complicated issue of the scaling of the dimensionless  $\langle k_x^2 \rangle$  with  $\rho_* = \rho_s/a$ . For localized turbulent eddies  $\langle k_x^2 \rangle$  is independent of  $\rho_*$ ; however, for radially extended eddies and vortices  $\langle k_x^2 \rangle$  scales approximately linearly with  $\rho_*$ . There is direct evidence of the

radially-extended vortices and eddies in the global 3D simulations.<sup>16,19-21</sup> The gyrofluid study of Garbet and Waltz<sup>22</sup> shows evidence for the extended eddies for  $R/L_{T_i}$  close to  $(R/L_{T_i})_c$ . Here we must make a choice: for simplicity and generality we choose the  $\mathcal{O}(\langle k_x^2 \rho_s^2 \rangle) \sim 1$  scaling describing the  $\rho_s$ -scale eddies and vortices. The semianalytic method described here for propagating  $W$  between transport time steps applies to both the Bohm (mesoscale eddies) and the gyroBohm (microscale eddies) transport regimes.

By separating the variables of Eq. (11) we readily integrate between the transport times  $t_j$  to  $t_{j+1}$  with frozen values of  $\gamma^l$  and  $\gamma^{nl}$ . The result of the analytic integration of Eq. (11) for  $W$  is that the update of the turbulence at  $x_i, t_j$  to  $x_i, t_{j+1}$  is given by

$$W(x_i, t_{j+1}) = R_i^j W(x_i, t_j), \quad (12)$$

where

$$R_i^j = \frac{\Gamma_i^j \exp(\Gamma_i^j)}{\Gamma_i^j + \Gamma_{1i}^j W_i^j (\exp(\Gamma_i^j) - 1)}, \quad (13)$$

where

$$\Gamma_i^j = \gamma_0 (t_{j+1} - t_j) \gamma^l(u, u', u'') \quad (14)$$

and

$$\Gamma_{1i}^j = \gamma_0 (t_{j+1} - t_j) \gamma^{nl}(u, u', u''). \quad (15)$$

Since the factor  $\gamma_0$  is very large, the value of  $R_i^j W_i^j$  reduces to the nonlinear saturation level  $\Gamma_i^j / \Gamma_{1i}^j = \gamma^l / \gamma^{nl} \equiv \hat{\gamma}^l / \langle k_x^2 \rangle$  except near the critical condition bifurcation regions  $\gamma^l \rightarrow 0$ . From Eq. (8) this condition occurs at the bifurcation where the shear flow  $Y_s^2$ -term builds up to balance the growth from  $R/L_{T_i}$ . For  $|\Gamma_i^j| \ll 1$ ,  $R \rightarrow 1$  and for  $\Gamma_i^j \ll -1$  the turbulence decays to an exponentially small value during the time  $t_{j+1} - t_j$ . This rapid adjustments of  $W$ , and thus of  $\chi$ , between the transport time steps provides the theoretical basis for the piecewise continuous  $\chi(u')$  models in Eqs. (34) and (37).

With the algorithm in Eqs. (12)–(15) the turbulence in the linearly stable domains decays to an exponentially small value. However, both the theory of radial convective wave propagation and the observations of the 3D simulations show that there remains a significant turbulence in linearly stable regions. To describe the radial propagation  $v_g$  and possible small diffusive transport of the turbulence we update the  $W_i^j$  with the finite difference formula for  $v_g > 0$ ,

$$W_i^{j+1} = \frac{W_i^j + \frac{v_g \Delta t}{\Delta \rho} W_{i-1}^j + \frac{\mu_W \Delta t}{(\Delta \rho)^2} (W_{i+1}^j + W_{i-1}^j)}{1 + \frac{2 \mu_W \Delta t}{(\Delta \rho)^2} + \frac{v_g \Delta t}{\Delta \rho}} \quad (16)$$

derived from the first-order upwind derivative for the convective transport of  $W$  and the diffusive transport from  $\mu_W$  in the absence of growth and damping.

The algorithms (12) and (16) give fast, practical rules for calculating the growth/decay and propagation of the turbulence between each transport time step  $\Delta t = t_{j+1} - t_j$ .

## B. Mass flow dynamics

The surface flows  $\mathbf{u}_a(\mathbf{x}, t)$  in tokamak are specified by two alternative and equivalent sets of flux functions. The most familiar set of flux functions are  $\langle Bu_{\parallel} \rangle$  for the parallel flow and

$$\left( E_r - \frac{1}{e_i n_i} \frac{\partial p_i}{\partial r} \right) / RB_p = - \frac{\partial \Phi}{\partial \psi} - \frac{1}{e_i n_i} \frac{\partial p_i}{\partial \psi} \quad (17)$$

for the perpendicular flow  $\langle Bu_{\perp a} / RB_p \rangle$ . Here  $\psi$  is the poloidal flux function with  $d\psi = RB_p dr_{\perp}$ . Alternatively, there are the geometrical representations of the flow given by the toroidal  $u_{T_a}$  and poloidal  $u_{p_a}$  velocities with flux functions given by

$$\langle B_p u_p \rangle = \langle \mathbf{B}_p \cdot \mathbf{u}_a \rangle \quad \text{and} \quad \langle B_T u_T \rangle = \langle \mathbf{B}_T \cdot \mathbf{u}_a \rangle. \quad (18)$$

The transformation between the two representations is given by

$$\langle B_p u_p \rangle = \frac{\langle B_p^2 \rangle}{\langle B^2 \rangle} \left[ \langle Bu_{\parallel} \rangle + \left\langle \frac{B_T}{B_p} Bu_{\perp} \right\rangle \right], \quad (19)$$

$$\frac{\langle B^2 \rangle \langle Ru_T \rangle}{\langle RB_T \rangle} = \langle Bu_{\parallel} \rangle - (1 + 2\hat{q}^2) \frac{\langle R^2 \rangle \langle B_p^2 \rangle}{\langle RB_T \rangle^2} \left\langle \frac{B_T}{B_p} Bu_{\perp} \right\rangle, \quad (20)$$

where

$$\hat{q}^2 = \frac{1}{2\langle B_p^2 \rangle} \left( \langle B_T^2 \rangle - \frac{\langle RB_T \rangle^2}{\langle R^2 \rangle} \right). \quad (21)$$

Now, Lorentz force equation for the flow velocity  $\partial \mathbf{u} / \partial t$  naturally breaks up into equations for the parallel flow velocity and the toroidal flow changes on the transport time scale while the parallel flow changes more rapidly.

Here we briefly summarize the results of the lengthy calculations required to determine  $\langle u_{\parallel B} \rangle$  and  $E_r / RB_p$ . The complete balance equation is

$$m_a n_a \frac{\partial \mathbf{u}_a}{\partial t} = n_a e_a \left( \mathbf{E} + \frac{1}{c} \mathbf{u}_a \times \mathbf{B} \right) - \nabla p_a - \nabla \cdot \boldsymbol{\pi}_a + \mathbf{F}_a + \mathbf{K}_a, \quad (22)$$

where  $\mathbf{F}_a$  and  $\mathbf{K}_a$  are the collisional friction force and the turbulent force respectively. The summation of surface averaged parallel flow equations gives

$$\begin{aligned} \frac{\partial}{\partial t} \sum_a n_a m_a \langle Bu_{\parallel a} \rangle &= - \sum_a \langle \mathbf{B} \cdot \nabla \cdot \boldsymbol{\pi}_a^{\text{neo}} \rangle \\ &\quad - \sum_a \langle \mathbf{B} \cdot \nabla \cdot \boldsymbol{\pi}_a^{\text{anom}} \rangle. \end{aligned} \quad (23)$$

Here  $\boldsymbol{\pi}_a^{\text{neo}}$  is the neoclassical stress tensor due to collision, while  $\boldsymbol{\pi}_a^{\text{anom}}$  is the anomalous stress tensor due to turbulence ("Reynold stress"). A simplified version of the surface averaged parallel component of the neoclassical stress tensor  $\boldsymbol{\pi}_a^{\text{neo}}$  is given in Yushmanov *et al.*<sup>23</sup> as

$$\begin{aligned} \sum_a \langle \mathbf{B} \cdot \nabla \cdot \boldsymbol{\pi}_a \rangle &\equiv \langle \mathbf{B} \cdot \nabla \cdot \boldsymbol{\pi}_i \rangle, \\ &= 3 \mu_{i1} \langle (\hat{\mathbf{n}} \cdot \nabla \mathbf{B})^2 \rangle \\ &\quad \times \left( \frac{\langle B_p u_{ip} \rangle}{\langle B_p^2 \rangle} + \frac{\mu_{i2}}{\mu_{i1}} \frac{\langle RB_T \rangle}{\langle B^2 \rangle} \frac{c}{e_i} \frac{dT_i}{d\psi} \right) \\ &= 3 \mu_{i1} \frac{\langle (\hat{\mathbf{n}} \cdot \nabla \mathbf{B})^2 \rangle}{\langle B^2 \rangle} \\ &\quad \times \left( \langle Bu_{\parallel i} \rangle + \left\langle \frac{B_T}{B_p} Bu_{\perp i} \right\rangle \right) \\ &\quad + \frac{\mu_{i2}}{\mu_{i1}} \langle RB_T \rangle \frac{c}{e_i} \frac{dT_i}{d\psi}. \end{aligned} \quad (24)$$

The function  $\mu_{i1}$  is usually approximated as

$$\mu_{i1} \approx \frac{n_i m_i R q v_{T_i} \nu_{*i}}{(1 + \nu_{*i})(1 + \epsilon^{3/2} \nu_{*i})}, \quad (25)$$

$\nu_{*i} = \nu_i R q / \epsilon^{3/2} v_{T_i}$ , and the average-squared mirror force is

$$\frac{\langle (\hat{\mathbf{n}} \cdot \nabla \mathbf{B})^2 \rangle}{B^2} \approx \frac{\epsilon^2}{2R^2 q^2}. \quad (26)$$

With the above formulas the equation for the fast parallel flow adjustment to track the transport time scale evolutions of  $dT_i / dr$  and  $u_{\perp B} \approx E_r$  is

$$\begin{aligned} \frac{\partial u_{\parallel i}}{\partial t} &= - \nu_{nc} \frac{B_p}{B_T} \left( u_{i\perp} + \frac{B_p}{B_T} u_{\parallel i} + \frac{\mu_{i2}}{\mu_{i1}} \frac{c}{e_i B_p} \frac{dT_i}{dr} \right) \\ &\quad - \frac{1}{n_i m_i B} \sum_a \langle \mathbf{B} \cdot \nabla \cdot \boldsymbol{\pi}_a^{\text{anom}} \rangle, \end{aligned} \quad (27)$$

where

$$\begin{aligned} \nu_{nc} &\equiv \frac{3}{2} \frac{q v_{T_i} \nu_{*i}}{R(1 + \nu_{*i})(1 + \epsilon^{3/2} \nu_{*i})} \\ &\equiv \frac{3}{2} \frac{B_T^2}{B_p^2} \frac{\epsilon^{1/2} \nu_i}{(1 + \nu_{*i})(1 + \epsilon^{3/2} \nu_{*i})}. \end{aligned} \quad (28)$$

The turbulent stress can be written as

$$\frac{1}{n_i m_i B} \langle \mathbf{B} \cdot \nabla \cdot \boldsymbol{\pi}_i^{\text{anom}} \rangle = \frac{1}{B} \langle \nabla \cdot \langle \tilde{\mathbf{v}} \tilde{\mathbf{v}} \rangle \cdot \mathbf{B} \rangle \approx \frac{\partial}{\partial x} \langle \tilde{v}_x \tilde{v}_{\parallel} \rangle \quad (29)$$

a transport flux which has been analyzed in detail in Dong *et al.*<sup>24</sup>

To determine the radial electric field  $E_r$ , one also needs to know the profile of toroidal velocity. The toroidal momentum transport equation is given in Eq. (6), where the viscosity is dominated by turbulent contribution, i.e.,  $\Pi_a \approx \Pi_a^{\text{anom}}$ . With the profiles of toroidal and parallel flow, the  $E_r$  profile can be obtained by the radial momentum balance equation

$$E_r = u_{\phi i} B_{\theta} - u_{\theta i} B_{\phi} + \frac{1}{Z_i n_i} \frac{dp_i}{dr}, \quad (30)$$

where the poloidal flow  $u_{\theta i}$  is obtained from parallel flow  $u_{\parallel i}$  by the incompressibility constraint. For plasma with large toroidal rotation, the radial electric field  $E_r$  can be simply determined by the toroidal velocity.

### C. Model diffusivities

In the toroidal flux coordinate form with  $x = \rho^2 = r^2/a^2$  the vector transport equations are of the form

$$\frac{\partial \mathbf{u}}{\partial t} = - \frac{\partial}{\partial x} [x \mathbf{J}(\mathbf{u}, \mathbf{u}', x, t)] + P \mathbf{S}(x, t) - \mathbf{S}_{\text{SOL}}(x, t), \quad (31)$$

where

$$\mathbf{J} = - \chi_x \cdot \frac{d\mathbf{u}}{dx}.$$

The detailed physical form of Eq. (31) is given in Sec. IV. Here  $\mathbf{u}$ ,  $\mathbf{J}$ , and  $\mathbf{S}$  are  $n_d$  dimensional vectors and  $\chi_x$  is a  $n_d \times n_d$  matrix. While the noncircular geometric parameters like elongation have strong influence on the tokamak confinement as shown for example in Bateman *et al.*,<sup>25</sup> here we focus on the nongeometric mechanisms of the transport barrier dynamics by considering equilibrium with circular magnetic surfaces. In Eq. (31) we introduce the core localized unit source function  $\mathbf{S}(x, t) = \mathbf{F}(t)S(x)$  such that  $\int_0^{x_{\text{max}}} dx S(x) = 1$ . Then  $P$  is the dimensionless constant determining the net injected power. The dimensionless power  $P$  is related to the dimensional auxiliary heating power  $P_{\text{aux}}$  in megawatt through

$$P = \frac{P_{\text{aux}} \tau_L}{(2\pi R)(\pi r_{dp}^2)(\frac{3}{2} n_0 T_0)}, \quad (32)$$

where  $T_0$  is the reference temperature and  $n_0$  the reference density. Here  $r_{dp}$  is the maximum deposition radius of  $P_{\text{aux}}$ . Thus,  $P_{\text{aux}}/(2\pi R)(\pi r_{dp}^2)n_0$ , is the heating rate per ion in keV/s with typical high powered devices having the rate of 30–100 KeV/s. For a plasma with  $\tau_L \approx 0.5$  s and  $T_0 = 1$  keV and  $3n_0/2 = 10^{20}/\text{m}^3$  this gives the range of  $P = 1 - 20$  for the dimensionless  $P$  in Eq. (32). The auxiliary power increases with the plasma volume. One may roughly take the value of  $P$  to be the power in megawatts for a JT-60U (Ref. 26) or Joint European Torus (JET) size device.

To absorb the power transported past the  $\rho = 1$  surface we use a scrape-off layer (SOL) sink  $\mathbf{S}_{\text{SOL}}(x, t)$  localized to  $1 \leq \rho \leq \sqrt{2}$ . The sink  $\mathbf{S}_{\text{SOL}}(x, t)$  is such that all power emitted from the core is absorbed by the SOL sink function. Reference values for the width of SOL sink is fixed at  $\Delta x_{\text{SOL}} = 0.3$  while that of the source is taken as either  $\Delta x_p = 0.1$ . The current version of TBD uses a strong scrape-off-layer (SOL) diffusivity from Connor *et al.*<sup>27</sup> in the zone  $1 \leq \rho \leq \sqrt{2}$  which makes the results more realistic and avoids the somewhat sensitive choice of the  $\mathbf{S}_{\text{SOL}}$  function.

In the empirical description of different confinement modes it has been useful to describe the thermal diffusivity by piecewise continuous functions. One fascinatingly complex example of a transport simulation that requires multiple steps in the electron diffusivity is the Rijnhuizen Tokamak Project (RTP) (Ref. 28) tokamak ( $I_p = 150$  kA,  $B_T = 2.5$  T,  $R/a = 0.72$  m/0.164 m) with electron cyclotron heating (ECH) that is well localized (deposition profile width  $\Delta \rho_{\text{dep}} \approx 0.1$ ). The electron temperature profile is accurately measured with a 20-channel electron cyclotron emission

(ECE) radiometer and an 80-channel soft x-ray (SXR) tomography system. There is also a double-pulse Thomson scattering diagnostic system that gives space–time resolution of 3 mm (the space resolution  $\Delta \rho_{\text{res}} \approx \Delta \rho_{\text{dep}}/5 \approx 0.02$ ) and the time resolution  $\Delta t_{\text{res}} = 0.8$  ms. The electron temperature profile shows a series of up to five flat annuli separated by four transport barrier regions. The space–time evolution of  $T_e(r, t)$  is reproduced by choosing a notched  $\chi_e(q(r, t)) = \chi_L$  profile with a base level of  $\sim 10$  m<sup>2</sup>/s between the integer and half-integer values of  $q$  and barrier set of low values  $\chi_e = \chi_H \lesssim 1$  m<sup>2</sup>/s around the integral and half-integral values of  $q$ . The width  $\Delta \rho_H$  of the low values of  $\chi_e$  is also adjusted. We do not attempt here to model these experiments in detail; however, we note that the drift wave map transport model<sup>29,30</sup> yields electron diffusivities that are sharp functions of the electron-wave phase relationship which changes at the rational surfaces. Thus, there are fundamental theoretical models that support the use of abrupt changes in the diffusivity on the transport space scale.

In view of the large number of  $e$ -foldings from the linear growth rate  $\gamma'(\{u\})$  during the transport time scale  $\tau_L$ , it is common to consider reduced, Markovian models of the nonlinear fluxes  $\mathbf{J}$  as local functions of the driving gradients  $\mathbf{u}'(x, t) \equiv \nabla_x \mathbf{u}(x, t)$  and  $\mathbf{u}(x, t)$ . While this time-local relationship between  $\mathbf{J}$  and  $\mathbf{u}'$  misses the details of the microscopic bifurcations<sup>11</sup> surrounding the critical points, the local relation captures the essential feature of the multivaluedness of the possible gradients  $\mathbf{u}'$  for a given radial flux  $\mathbf{J}$ . A parameterization of the nonlinear diffusivity that includes the models of Hinton and Staebler<sup>31,32</sup> and other models found in the literature is

$$\chi = \chi^{nl}(W) + \chi_{\text{neo}}, \quad (33)$$

$$\chi^{nl} = \frac{\chi_L}{1 + (u'/u'_c)^n},$$

with the parameters  $n$  and  $u'_c$  specifying the particular model. Here  $\chi_L \gg \chi_{\text{neo}}$ , where  $\chi_L$  is the L-mode turbulent thermal diffusivity and  $\chi_{\text{neo}}$  is the neoclassical diffusivity. The turbulence determines the L-mode (low confinement mode) diffusivity in the limit of weak  $E_r$ -shear. The mechanism for the nonlinear  $\chi^{nl}(W)$  is expressed in Eq. (33) by the strength of the density gradient ( $u'_1$ ) or the temperature gradient ( $u'_2$ ) creating a sheared  $\mathbf{E} \times \mathbf{B}$  flow in the plasma. The reduction occurs for  $|u'| > u'_c$  and the sharpness of the transition between  $\chi_L$  and  $\chi_{\text{neo}}$  increases with  $n$ . The case  $n=2$  is based on the  $\chi$ -reduction from shear flows as given in Shaing *et al.*<sup>33</sup> The Biglari–Terry–Diamond<sup>34</sup> work gives  $n=2/3$ , but later Carreras *et al.*<sup>6</sup> change to the  $n=2$  exponent. Zhang and Mahajan<sup>35</sup> obtain a strong suppression function which can be modeled with  $n=4$ .

While  $n=2$  can give a bifurcation, we find that the  $n=2$  exponent gives too weak a dependence for  $\chi(u')$  to reproduce the relatively strong temperature profile effects observed in the experiments. A model with  $n=4$ , however, produces a stronger transition closer to the experiments. The motivation for the  $n=4$  model is given by nonlinear form of the turbulent  $\chi(L_s v'_E/c_s)$  in Fig. 7 of Hamaguchi and Horton<sup>12</sup> which shows a flat  $\chi(L_s v'_E/c_s)$  at small  $v_E$ -shear

TABLE I. Transport models.

Case	$\chi$ -model	$P_{\text{crit}}$	$H$	Figures	Run
A	Eq. (34) switch	15	1.13	1(a)–1(d)	796z
B	Eq. (33) $n=4$	$\sim 7$	1.7	2(a)–2(d)	796m2
C	Eq. (33) $n=2$	continuous	1.2	3(a)–3(f)	796q
D	type-II barrier Eq. (38)	$\leq 10$	1.5	4(a)–4(g)	784b

flow with a rapid drop-off of the diffusivity at  $L_s v_E' / c_s > 2$ . Formula (33) with  $n=4$  is taken as our reference model since it gives a strong enough change of slope in the temperature profile to model the transport experiments with type I barriers. The origin of the stronger nonlinear  $\chi(u')$  dependence is also understood from the  $\chi = \chi_0 W(r, t)$  dependence on the turbulence level  $W$  with  $W \rightarrow W^{nl}(u')$  being a strong function of  $u'/u_c'$  through the growth rate. Here  $W(r, t)$  is the low-frequency drift wave turbulent energy density in the plasma.<sup>18</sup>

An idealized model found useful in the simulations developed here is based on the evolution of the turbulence  $W$  which has a very sharp variation with  $u'$  due to the exponential dependence of  $W$  on  $\gamma'(u')\tau_L$ . This exponential dependence is modeled by

$$\chi = \begin{cases} \chi_L & \text{for } -u' < u_c' \\ \chi_H & \text{for } -u' > u_c' \end{cases} \quad (34)$$

as discussed in Sec. III. Here we have taken  $u_c'$  as positive. In this model the smoothing of  $W(r)$ , and thus  $\chi$ , due to the finite radial correlation length  $\lambda_c$  and radial wave propagation is neglected. As a result the jumps in  $-du/dx$  at  $\rho_{\text{ITB}}$  are stronger than for the more complete model given in Sec. III with radial propagation of the turbulence. We find, however, that the density and temperature profiles appear consistent with those reported in Koide *et al.*<sup>1</sup> and Levinton *et al.*<sup>36</sup> Now we discuss the properties of these models. We began the use of the piecewise continuous  $\chi$  formulas in Eq. (34) in 1997 before learning of their successful use in modeling the RTP tokamak temperature profiles.<sup>28</sup> We were also motivated by the guiding center test particle transport properties.

A fundamental process by which the model in Eq. (34) is suggested is from the test particle simulations. For low collision frequency the invariant KAM surfaces begin to emerge and produce dramatic jumps in the test particle guiding center diffusivities.<sup>29,30,37</sup>

## IV. SIMULATION RESULTS OF TRANSPORT MODELS

### A. Performance with the linear flux-gradient transport model

The linear flux-gradient relation of  $J/(-du/dx) = D = \text{constant}$  gives the stored energy  $W_s \propto P$ , and thus the confinement time  $\tau_E = W_s/P$ , is independent of  $P$  and given by  $\tau_E \cong 0.55\tau_L/\chi_x = 0.14a^2/\chi_r$ , where we use  $\chi_x = 4\chi_r[a^2/\tau_L]$  due to the factor of four that occurs from the transformation  $dx = 2rdr/a^2$  in the transport equation. Here  $\chi_r$  is the usual dimensional diffusivity in  $m^2/s$ , for example, and  $\chi_x$  is the dimensionless diffusivity.

For the linear flux-gradient model the shape of the steady state  $u(x)$  varies approximately such that the maximum gradient  $u'_{\text{max}}$  varies as

$$-u'_{\text{max}} \cong 0.65P/\chi_x \Delta x_p, \quad (35)$$

and the core temperature increasing as

$$u(0) \cong 0.6P/\chi_x \sqrt{\Delta x_p}, \quad (36)$$

where  $\Delta x_p$  is the width of the power deposition profile in  $r^2/a^2$ . Thus, for sufficiently large  $P/\Delta x_p$  the critical gradient  $u_c'$  is exceeded (in the linear flux model) for the onset of the multivalued  $u' = u'(J)$  relation. For nonlinear (anomalous) diffusivities, however, the increase of the gradient  $-u'$  with  $P$  may be much slower, such as  $P^{1/2}$ , and the bifurcation condition is more difficult to determine.

### B. Nonlinear flux-gradient transport

We present four cases, A–D, of transport barriers with increasing complexity. Table 1 summarizes the cases and gives the H-factors for the highest  $P$  value,  $P=20$ . For each model we focus on the evolution of ion temperature transport equation (i.e.,  $\mathbf{u}(\rho, t) = (0, 0, u_3(\rho, t), 0) = (0, 0, T_i(\rho, t), 0)$ ) and apply the dimensionless power  $P = 1, 5, 10$ , and 20. Some models show a clear critical power  $P_{\text{crit}}$  and others show a continuous improvement in confinement.

*Case A:* Figure 1(a) shows the  $u_3$ -profiles reached after six  $\tau_L$ -times for the four (dimensionless) power levels of  $P = 1, 5, 10$ , and 20 using the simple switch rule in Eq. (34) with  $\chi_L = 1$  and  $\chi_H = 0.5$  and  $u_c' = 30$ . Subsequently, in Cases B and C, we compare these results with those for the continuous nonlinear model in Eq. (33) for both  $n=2$  and  $n=4$  models. For the  $P=20$  curve, the break in the slope of  $u(x)$  is just visible in Fig. 1(a) at  $\rho \approx 0.5$ .

On the next page in Fig. 1(b) the evolution of the energy confinement time  $\tau_E = W_s/P$  for different input power is shown. The effect of the bifurcation for the highest ( $P=20$ ) case is a modest  $\tau_{\text{ITB}}/\tau_0 = 0.44/0.39 = 1.33$  H-factor. This transition is not as strong as that observed in the typical measured temperature profiles.

The bifurcations show up much more clearly in Fig. 1(c), showing the radial flux  $J$  vs the value of  $-du/dx$  and in Fig. 1(d) showing the radial profiles of  $-du/dx$ . Here, it is clear that the highest power level  $P=20$  is sufficient to create slopes above that required for the bifurcation from  $\chi_L$  to  $\chi_H$  while the three lower powers levels are below the critical power. The critical power is approximately  $P_{\text{crit}} = 0.4u_c'$  in this model [with  $P$  given by Eq. (32)].

The rapid change in the gradient  $-u'$  is shown in Fig. 1(d) for the barrier region  $\rho \approx 0.55$  and is well resolved in both space and time by the simulation. The radial spacing is  $\Delta\rho = \Delta x/2\rho \approx 10^{-2}$  in the region of the barrier and the average adaptive time step is  $\Delta t \cong 10^{-3}\tau_L$  during the evolution.

*Case B:* Now, we repeat this simulation with the continuous nonlinear diffusivity in Eq. (33). First, for  $n=4$  and  $u_c' = 40$ , and  $\chi_L = 1$  we add the low level of background flux with  $\chi_H = 0.5$  so that the net flux is

$$J = -\chi^{nl}(u')u' - \chi_H u'. \quad (37)$$

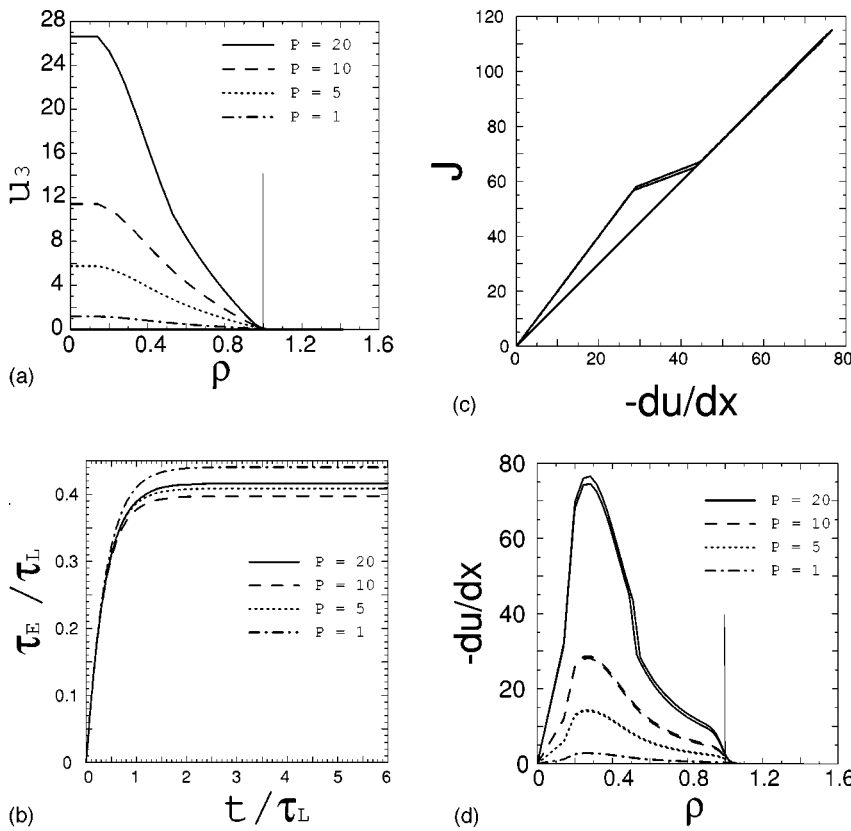


FIG. 1. (a) The final state profiles of  $u_3(\rho, t)$  at  $t=6\tau_L$  produced by the piecewise discontinuous  $\chi(u')$  model in Eq. (34) with  $\chi_L=1$ ,  $\chi_H=0.5$ , and  $u'_c=30$  (Case A) for dimensionless powers  $P=1, 5, 10, 20$ , where the one with the highest power level exceeds the critical gradient  $\rho \approx 0.55$ . (b) The evolution of energy confinement time of  $u_3$  for dimensionless powers  $P=1, 5, 10, 20$  in Case A. The confinement times  $\tau_E$  showing the enhancement factors for  $P=20$  where a bifurcation occurs from the base level  $L$ -mode confinement. The transport barrier formed for  $P=20$  has the confinement time improved by the  $H$ -factors of  $H=1.16$ . (c) The nonlinear flux  $J$  vs the gradient  $-u'$  for all four power levels in Case A. The highest power level produces a gradient above the critical gradient with a hysteresis loop. (d) Evolution of the gradients for four power levels  $P=1, 5, 10, 20$  used in (a), with curves of two time slices for each power case at  $t=3\tau_L$  and  $t=6\tau_L$  in case A. For  $P=20$  case the gradient  $-u'(\rho, t)$  profile showing clearly the transport barriers formed where  $u'$  exceeds the critical gradient  $u'_c=30$  at  $\rho_{ITB}=0.56$ .

The  $J(u')$  function is  $S$ -shaped with the standard two stable fixed points at low and high gradients and the intermediate unstable fixed point at a moderate gradient. The plots corresponding to Figs. 1(a)–1(d) are shown in Figs. 2(a)–2(d).

Figure 2(a) shows the evolution of the  $u_3$  profiles and Fig. 2(b) the energy confinement time. The results for the  $n=4$  model show a clear transport barrier formation at  $P=10$  (the ITB position  $\rho_{ITB}=0.45$ ) and  $P=20$  ( $\rho_{ITB}$

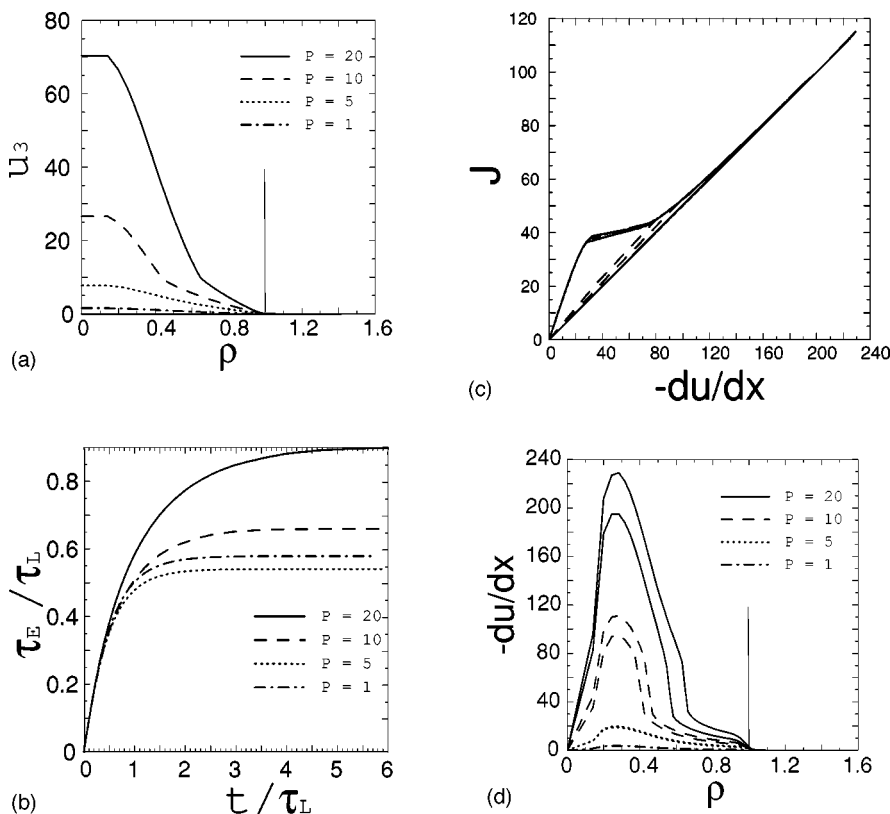


FIG. 2. (a) The final state profiles of  $u_3(\rho, t)$  at  $t=6\tau_L$  for  $n=4$ ,  $u'_c=40$  (Case B) with the  $\chi_L$  with dimensionless powers  $P=(1, 5, 10, 20)$ . The two highest power levels produce ITBs at  $\rho=0.44$  for  $P=10$  and  $\rho=0.65$  for  $P=20$ . (b) The evolution of energy confinement time of  $u_3$  for dimensionless powers  $P=1, 5, 10, 20$  in Case B. Confinement times showing  $\tau(P=1) = \tau(P=5) \approx 0.55$  and  $\tau(P=10) = 0.65 = 1.18\tau(P=1)$  and  $\tau(P=20) = 0.9 = 1.64\tau(P=1)$ . (c) The nonlinear flux  $J$  vs the gradient  $-du/dx$  for all four power levels in Case B. (d) The gradient  $-u'(\rho, t)$  for all power levels, with curves of two time slices for each power case at  $t=3\tau_L$  and  $t=6\tau_L$  in Case B.

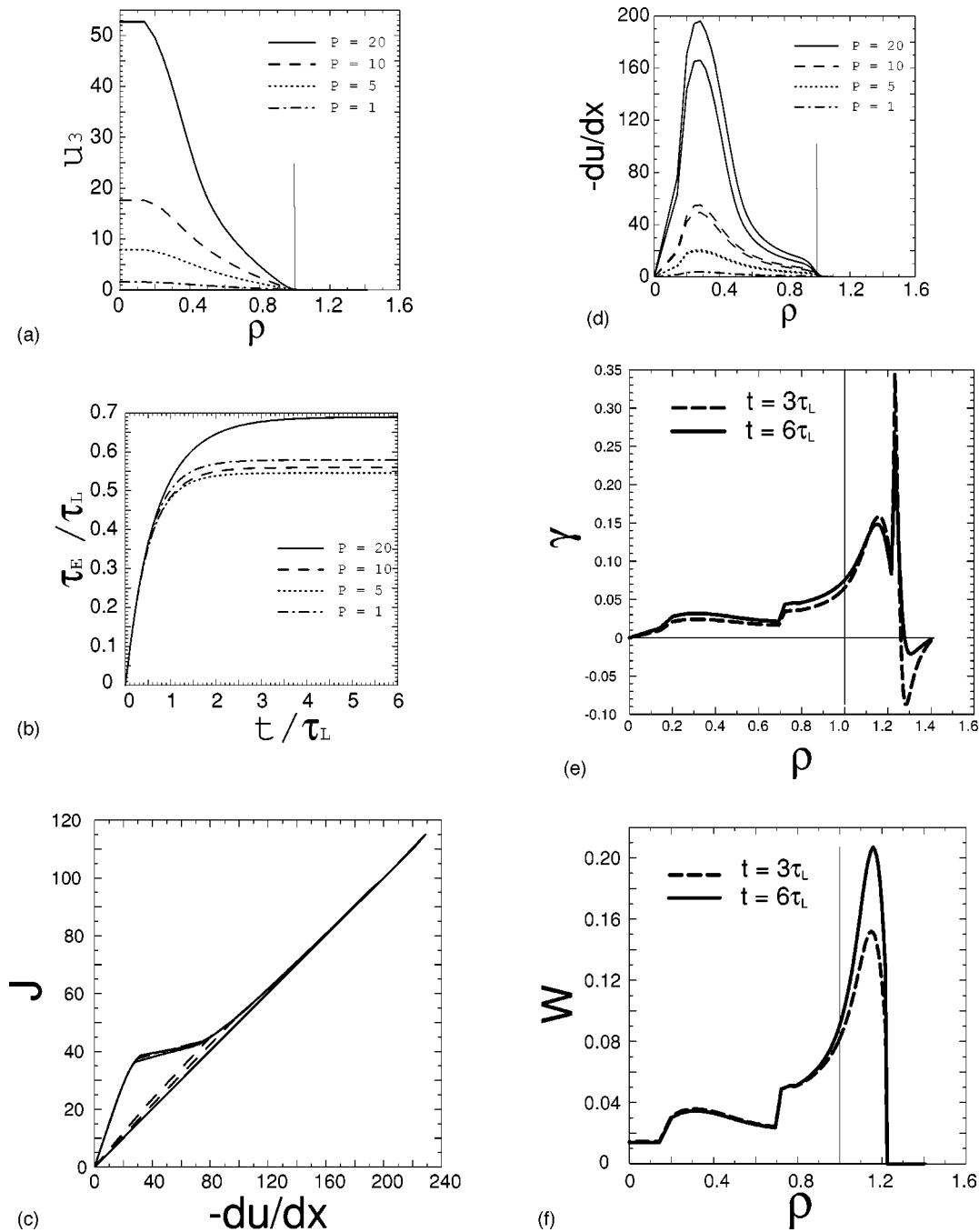


FIG. 3. (a) The final state profiles of  $u_3(\rho, t)$  at  $t = 6\tau_L$  for  $n = 2$ ,  $u'_c = 40$  with the  $\chi_L$  (Case C). Here  $P = (1, 5, 10, 20)$ . (b) The evolution of energy confinement time of  $u_3$  for dimensionless powers  $P = 1, 5, 10, 20$  in Case C. Only  $P = 20$  case has a confinement improvement. The enhancement factor is  $H \approx 0.69/0.56 = 1.2$ . (c) The nonlinear flux  $J$  vs the gradient  $-du/dx$  for all four power levels in Case C. (d) The gradient  $-u'(\rho, t)$  for all power levels, with curves of two time slices for each power case at  $t = 3\tau_L$  and  $t = 6\tau_L$  in Case C. (e) The model ITG growth rate computed from  $u_3$  profile for  $P = 10$  in Case C. (f) The turbulent energy density  $W(r, t)$  computed from gradient profile in Case C (e) with  $v_g = \mu_w = 0$ .

$= 0.65$ ). The H-factor is  $H \approx 0.90/0.53 = 1.7$  similar to many experiments. The flux versus gradient relation in Fig. 2(c) shows the phase transition characteristic of constant  $j$  for  $-u'$  in the range 25–60. For the highest power the  $H \approx 1.7$  as shown in Fig. 2(b). The model shows clear bifurcation at  $P_{crit} \approx 7$  with  $P = 10$  having  $\rho_{ITB} \approx 0.45$  and  $P = 20$  having  $\rho_{ITB} \approx 0.65$  in Fig. 2(d).

Case C: Now in Figs. 3(a)–3(f) the corresponding quantities for the  $n = 2$  model are shown. For this model, the improved confinement occurs only for the highest power,

$P = 20$ , value. The profiles show a more continuous change without a clear bifurcation point. The effect on the energy confinement time is weak. Thus, we conclude that the stronger nonlinear switching of the  $n = 4$  model and the piecewise discontinuous  $\chi$ -models are more representative of the experiments than the  $n = 2$  model.

Figure 3(a) shows the saturation of the  $u_3$  profiles for  $P = 1, 5, 10, 20$  at the time  $t_n = 6\tau_L$ . For this model there is no well-defined threshold power for the transport barrier. For the highest power level  $P = 20$  there is a substantial increase

in the gradient between  $\rho=0.7$  and  $\rho=0.4$  by a factor of approximately 5 as shown in Fig. 3(d). The highest power level also has a clear H-factor as shown in Fig. 3(b) of  $H=0.69/0.56=1.2$  for the  $\tau(P=20)/\tau(P=10)$  discharge simulations. Figure 3(c) for the flux vs the gradient shows a nonlinear shape but no clear phase transition comparable to that shown in Fig. 2(c) for the  $n=4$  model.

Figure 3(e) shows the growth rate computed from the logarithmic gradient of the  $u_3(\rho, t)$  profile in Case C. Clearly, the growth rate steps up beyond  $\rho \approx 1.1$ . There we see at least three phases of the turbulence. A low-base level in the core, 2–3 times the base level in the region  $\rho=0.2-0.7$  and then an abrupt increase from  $\rho=0.7$  to a maximum at  $\rho=1.1$  in the SOL. Echoing the discussion in Sec. II A of the turbulent energy density  $W(\rho, t)$  we show in Fig. 3(f) the associated turbulent energy density  $W(\rho, t)$  in this case.

Finally, we summarize that these first three cases A, B, C show the continuous type transition and the bifurcation type transition to the type I transport barrier. However, these models seem inadequate for modeling the type II transport barriers, an example of which is given in Ishida *et al.*<sup>4</sup> To obtain the type II barriers we introduce three  $\chi$ -level formulas.

### C. Type-II transport barriers

To obtain steady-state profiles with flat cores and very steep and localized gradients separating the core from the edge plasma we require that

$$\chi = \begin{cases} \chi_0 & \text{for } \rho < \rho_0 \\ \chi_H & \text{for } \rho_0 < \rho < \rho_{\text{ITB}} \\ \chi_L & \text{for } \rho > \rho_{\text{ITB}} \end{cases} \quad (38)$$

This example is labeled *Case D*. Recent particle simulations by Kishimoto *et al.*<sup>38</sup> strongly support the discontinuity model for internal transport barrier formation in reversed magnetic shear region. Simulations not shown with  $\chi_H = \frac{1}{2}\chi_0 = \frac{1}{2}\chi_L$  do not produce results qualitatively different from those shown in Fig. 3. Thus, we are led to consider a high core diffusivity  $\chi_0 = \chi_L \gg \chi_H$ . The large value of the required core  $\chi_0$  suggests that a qualitatively different transport mechanism operates in the core. Koide *et al.*<sup>39</sup> state that the flat temperature profiles near the axis, as in shot E27969, and other type-II discharges are not due to the hollow power deposition but to the degradation of transport in the core. Candidates for the high core diffusivity  $\chi_0$  would be a small scale magnetic stochasticity or a Bohm diffusivity perhaps from exceeding the low- $n$  kinetic stability threshold. Within the framework of this simple model the values  $\chi_0=10$ ,  $\chi_H=0.5$ , and  $\chi_L=5.0$  give a reasonable representation of the type-II profiles. The results for this Case D simulation are shown in Figs. 4(a)–4(g).

Figure 4(a) shows the final state profiles for the model with a power ramp in  $P(t)$ . Figure 4(b) shows the evolution of the time dependent energy confinement times  $\tau_E(t) = E(t)/P(t)$  for  $P(t) = PF(t) = (1, 5, 15, 20) * F(t)$ , where the power ramp function  $F(t)$  is shown on the right axis. There is a bifurcation between  $P=5$  and  $P=15$  which is clearly

shown in both Figs. 4(a) and 4(b). Above the bifurcation both  $P=15$  and  $P=20$  have an H-factor at the end of the high power phase of  $H=0.88/0.60=1.5$ .

Figure 4(d) shows the profiles of the gradients with two high gradient regions. In Fig. 4(e) the time traces are the ion temperature at evenly-spaced positions in  $x_i = \rho_i^2$  with  $\Delta x = 0.2$  and  $x_i = 0$  to 2.0. The gap that opens between the temperature at  $x=0.4$  and  $x=0.6$  is the typical experimental signature of a transport barrier.

Figure 4(f) shows the growth rate computed from Eq. (9) and Fig. 4(g) shows the turbulent energy density  $W(\rho, t)$  computed from Eq. (12) for Case D for the type-II transport barrier. We see that the turbulence level in the steep gradient regions is suppressed more than in Case C shown in Fig. 3(f).

The three-zone transport model of  $\chi$  given in Eq. (38) with the choices of  $\chi_{\text{core}}=10$ ,  $\chi_{\text{ITB}}=0.5$  and  $\chi_{\text{edge}}=5$  and the  $P_i=20$  ( $\approx 20$  MW) and  $P_e=10$  ( $\approx 10$  MW) in the dimensionless units produces  $T_i$  and  $T_e$  profiles that are similar to those of the E27969 shot and E27302 shot in JT-60U. Here we use the same model for the transport coefficient  $\chi$  to both  $T_e$  and  $T_i$  channels, i.e., letting  $\mathbf{u} = (u_1, u_2, u_3, 0) = (n_e, T_e, T_i, 0)$ , while applying different powers for each by specifying  $PS = (S_e, P_e, P_i, 0)F(t)S(x)$ . Figure 5 shows the results for this simple simulation model for shot E27969 in JT-60U. Both these experiments have  $T_i(0)/T_e(0) \sim 2$ , as opposed to a temperature ratio of 3 in the type-I discharges, and the flat core temperature profiles. Other continuous model combinations of  $\chi$ 's were tried but the conclusion so far is that we need the large core  $\chi$  and the sharp drop in  $\chi$  in the ITB layer to account for the measured ion and electron temperature profiles.

More modeling using the ideas of large ion orbit effects<sup>37</sup> and or reversed magnetic shear effects on  $\chi$  will be required to narrow the range of mechanisms responsible for type-II transport barriers. The global simulations of Kishimoto *et al.*<sup>20,40</sup> suggest that an  $\mathbf{E} \times \mathbf{B}$  type of leaky Kolmogorov–Arnold–Moser (KAM) convective flow barrier is set up at the  $q_{\text{min}}$ -surface. This idea for the mechanism of establishing the reduced  $\chi$  at the  $q_{\text{min}}$  surface is fully supported by test particle simulations.<sup>29,30</sup> In contrast, the comprehensive 3D turbulence gyrokinetic simulations of Sydora *et al.*<sup>21</sup> indicate that such an  $\mathbf{E} \times \mathbf{B}$  barrier is a short-lived transient. In the fully developed turbulent state the Sydora *et al.*<sup>21</sup> reversed shear simulations show only weak changes in the transport perhaps consistent with a  $\chi_0 \sim \chi_L = 10\chi_{\text{ITB}}$  model. Thus, magnetic stochasticity or electromagnetic turbulence in the core plasma may be required to explain the type-II barriers.

Experimentally the electron transport barrier appears to be controlled by the magnetic shear reversal.<sup>4</sup> The reason for the strong dependence of electron transport on the  $q$ -profile is mostly easily understood from the test particle simulations.<sup>41</sup> The electron guiding center follows the magnetic field line with such a high speed ( $\sim v_{Te}$ ) that the influence of  $E_r$ -shear is weak. The electrons are also sensitive to the small scale  $c/\omega_{pe}$  and short time scale  $(L_{Te}R)^{1/2}/v_{Te}$  turbulence. Thus, the test particle simulations with reversed shear and high speed particles<sup>30</sup> show suppression of the

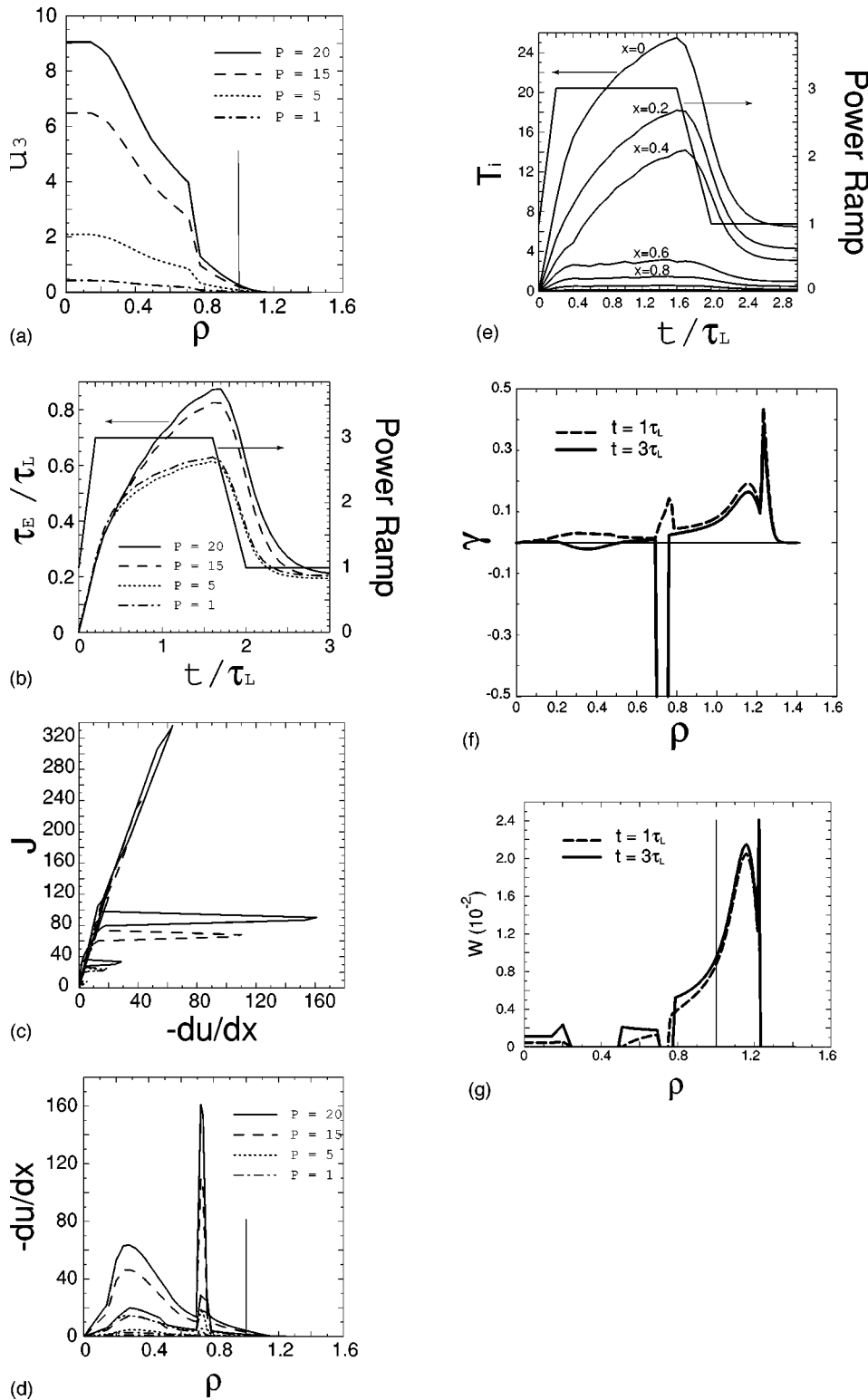


FIG. 4. (a) The final state profiles of  $u_3(\rho, t)$  at  $t = 3\tau_L$  for  $\chi_L = 5$ ,  $\chi_m = 0.5$  and  $\chi_H = 1.0$ ,  $\rho_0 = 0.71$ ,  $\rho_{ITB} = 0.77$  (Case D) with  $P = (1, 5, 15, 20)$ . (b) The evolution of energy confinement time of  $u_3$  for dimensionless powers  $P = 1, 5, 15, 20$  in Case D, together with the power ramping profile, showing the maximum  $H$ -factor shortly after the turn-down of the power with  $H \cong 0.88/0.60 = 1.5$ . (c) The nonlinear flux  $J$  vs the gradient  $-du/dx$  for all four power levels in Case D. (d) The gradient  $-u'(\rho, t)$  for all power levels, with curves of two time cases at  $t = 1\tau_L$  and  $t = 3\tau_L$  in Case D. (e) The time traces of the ion temperature at evenly-spaced  $x = \rho^2$  positions from plasma center to edge in Case D. The ITB gap opens and then closes with the power ramping up and down on the right side scale. (f) The model ITG growth rate computed from  $u_3$  profile for  $P = 15$  in Case D. (g) The turbulent energy density  $W(r, t)$  computed from gradient profile in Case D (e) with  $v_g = \mu_W = 0$ .

transport across the  $q$ -reversal layer by a factor of 1/5–1/10. Thus transport suppression is modelled here by dropping by 1/10 the core value of  $\chi$ .

**V. SCALING LAWS FOR THE ITB FORMATION**

The simulations of the transport barriers in Secs. IV suggest the following derivation of the characteristic scaling laws. The condition for the formation of an internal transport

barrier depends on (1) the deposited power  $P_{aux}$  and the characteristic deposition radius  $r_{dp}$  inside of which the bulk of the heating power is deposited, (2) the magnetic shear profile, and (3) the confinement law of the pre-existing turbulent plasma confinement  $\chi_L$ . In addition, a clear critical power  $P_{aux}$  is found only if the transport suppression model is sufficiently strong, as for example, for the  $n = 4$  model.

Keeping in mind these caveats, it is still instructive to

### Model of Internal Transport Barrier for JT-60U Shot E27969

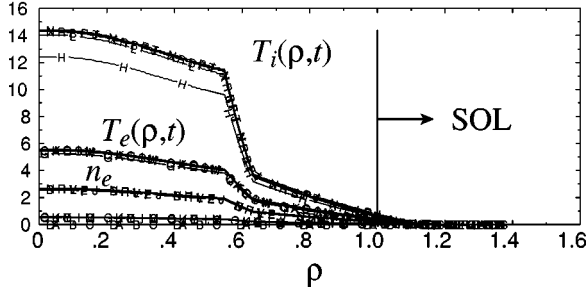


FIG. 5. The final state profiles obtained for the three-step diffusivity model chosen with appropriate diffusivities for the type-II internal transport barrier in the JT-60U deuterium experiment with an equivalent-fusion power  $Q$  near unity.

make the balances required to find the critical power required to create the gradients and  $E_r$ -shearing required to form a transport barrier. First we consider the case of the Bohm-type confinement and then the gyro-Bohm confinement.

The Bohm-type confinement is expected theoretically in large machines ( $1/\rho_* > 100$ ) when the  $E_r$ -shearing is low  $Y_s \ll 1$  and the  $q$ -profile is monotonic. We take the simple form of the Taroni–Bohm diffusivity

$$\chi = \chi_0 \frac{T_e a}{B} \frac{dT_i}{T_i dr} \quad (39)$$

with  $\chi_0 = 3 \times 10^{-4} q^2$  which is the baseline transport formula for the JET.<sup>16,17</sup> Here the  $q$ -scaling of  $\chi$  is disregarded, and we leave off the negative sign on  $dT_i/dr$  in Eq. (39) and in the following equations. Power balance in the ion channel requires

$$Sn\chi \frac{dT_i}{dr} = P_{\text{aux}}, \quad (40)$$

where  $S$  is the surface area just outside the deposition radius of the heating power  $P_{\text{aux}}$  for the ion power flow channel. The result of (39) and (40) is that the ion temperature gradient increases as

$$\frac{dT_i}{dr} = \left( \frac{P_{\text{aux}} B}{\chi_0 n a S \tau} \right)^{1/2}, \quad (41)$$

where  $\tau = T_e/T_i \approx \text{constant}$ .

Now we use the gradient formula (41) to determine the scaling of the dimensionless shearing parameter  $Y_s$ . We take the condition for the onset of the transport barrier to be  $Y_s > Y_c$ . We then find that the scaling of the threshold power for the ITB formation is

$$P_{\text{aux}}^c = \frac{\chi_0 Y_c^2 n B a^4 T_e}{R m_i} f\left(\frac{r_{dp}}{a}, \frac{s}{q}\right), \quad (42)$$

where the order unity function  $f$ , varies roughly as  $f = (s^2/q^2 + c_1)(r_{dp}/a)^2$ . The dependence of the function  $f$  needs further numerical exploration. More detailed simulation will be required to determine the  $f$ -function. For  $R/a = 3$  m/1 m,  $B = 4$  T,  $T_e = 10$  keV,  $\chi_0 Y_c^2 = 10^{-3}$ , formula

(42) gives about 10 MW. Note that  $1 \text{ T} = 1 \text{ V s/m}^2$ . Dimensional analysis then gives the generalization of Eq. (41) to

$$P_{\text{aux}}^c = e B n a^3 c_s^2 F(\mu) \chi_0 Y_c^2,$$

where  $n a^3$  is the number of particles in the system,

$$e B c_s^2 = 1.53 \times 10^{-8} B(T) T_e(\text{KeV}) / A_i \quad [\text{W}]$$

(here  $A_i$  is the atomic mass of the working gas and  $[\text{W}] = \text{watts}$  for the units of the equation),  $\chi_0 Y_c^2 \sim 10^{-4}$ , and  $F(\mu)$  is a dimensionless order unity function of the system parameter  $\{\mu\}$ .

The scaling formula (42) for the critical power is already interesting in that it shares some properties with empirical scaling law for the L to H transition critical power which is

$$P_H^{\text{emp}} = 0.04 n B S_a, \quad (43)$$

where  $S_a$  is the surface area at  $r = a$ . C-Mod, for example, finds formula (43) derived originally in ASDEX-U applies but with the lower numerical coefficient of 0.02.<sup>42</sup> Machines with reversed magnetic shear have achieved the transport barrier with lower critical power which is presumably consistent with lower value of  $f(s/q \rightarrow 0)$ . Finally, in the case of strongly rotating plasmas such as DIII-D and JET there may also be an additional toroidal velocity dependence of  $f$  not developed here.

For the pre-existing turbulent transport in the gyro-Bohm state the scaling law for formation of the barrier is rather different. Using  $\chi = \chi_{gB}(\rho_i/L_{Ti})(T_e/B)$  in Eq. (40) leads to the increase of the ion temperature gradient given by

$$\frac{dT_i}{dr} = \left( \frac{a}{\rho_s} \right)^{1/2} \left( \frac{P_{\text{aux}} B}{\chi_{gB} n a S \tau^{1/2}} \right)^{1/2}, \quad (44)$$

where  $\chi_{gB} \approx 0.3$  and  $T_e$  is taken as approximately constant.

Combining Eq. (44) with the critical shearing condition  $Y > Y_c$  yields the ITB power scaling law

$$P_{\text{aux}}^{c, gB} = \frac{n S a^2 c_s T_e}{R} f_{gB} \left( \frac{r_{dp}}{a}, \frac{s}{q} \right). \quad (45)$$

This scaling law is markedly different from the empirical scaling for the H-mode critical power in Eq. (43). Scaling laws for the ITB barrier formation are not known at this time so that both formulas (42) and (45) are still candidates for predicting the observed threshold scaling. To the extent that the internal barrier is similar to the L to H transition, the similarity of the Taroni–Bohm-based critical power scaling law in Eq. (43) with the empirical scaling law (43) adds evidence to the conclusion that the pre-existing plasma confinement is a Bohm-type confinement state. Working out the numerical values in the derivation leads to power levels of between 10–20 MW as shown earlier for JT-60U discharge 17110 in some detail.<sup>18</sup>

In both Eqs. (42) and (43) we leave  $T_e$  as a parameter to be taken from the experiments. For a complete description of scaling we must use the electron power balance channel and  $\chi_e$ . However, for the neutral beam injection (NBI) driven plasmas  $T_e$  is weakly varying with the system parameters; thus adding the complication of electron power balance with  $\chi_e$  and  $P_{\text{aux}}^e$  seems unwarranted at this stage of the analysis.

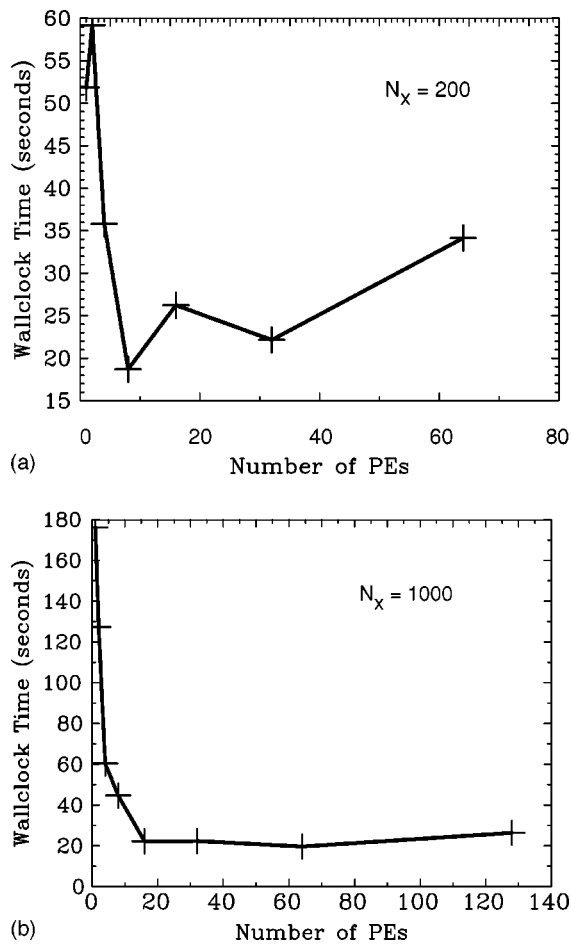


FIG. 6. The change of wallclock time as the number of processor elements increases when the number of radial grid points (a)  $n_x=200$ , (b)  $n_x=1000$ .

## VI. CONCLUSIONS

New simulations for the transport barrier dynamics are presented using the code TBD (transport barrier dynamics) developed for high resolution of the sharp radial gradients and the fast time dynamics that occur in the radial transport with bifurcations. The TBD code is in F90 with MPI instructions for parallel machines (Cray T3E). The code has been tested with a variety of nonlinear transport fluxes  $j(u, u')$ . The speed-up in wallclock time with increasing number of processing elements is shown in Fig. 6(a) for  $n_x=200$  radial grid points and in Fig. 6(b) for  $10^3$  radial grid points.

We define a new, dimensionless parameter  $P$  in Eq. (32) that characterizes the excess of the power injected over that required for the usual L-mode plasma confinement. We then show the confinement achieved for a number of different transport models with  $P$  increasing from unity to twenty. Barriers can be weak with no well-defined thresholds ( $n=2$  model) or sharp with a well-defined critical power  $P_{\text{aux}}^c$  ( $n=4$  and Case D). The  $n=4$  shear flow suppression formula appears to agree better with turbulence simulation<sup>12</sup> and the experimental profile<sup>1-4</sup> features of an ITB.

Typically only a limited radial range of plasma is in the improved confinement mode. As the power increases above the critical power  $P_{\text{aux}}^c$  the improved confinement zone ex-

pands radially as described in the tokamak experiments and in the theory of Lebedev and Diamond.<sup>9</sup>

We argue that test particle transport simulations allow the introduction of sharp changes in the thermal diffusivity due to the presence of partially broken Kolmogorov–Arnold–Moser (KAM) surfaces in the guiding center phase space. Thus, we introduce simple models with jumps in the value of the diffusivity across these KAM barrier zones and are then able to reproduce the temperature profiles of the type-II transport barriers found in JT-60U.

In Sec. V we develop the critical power scaling law implied by the transport barrier dynamics found in the simulations and compare with the empirical scaling laws. The example shown in Fig. 2(d) clearly shows the birth of the ITB in the inner zone ( $\rho \approx 0.4$ ) at the critical power and the subsequent outward radial motion of the footpoint with increasing values of the dimensionless power parameter. In the example shown the final footpoint increases from  $\rho=0.45$  to  $\rho=0.70$  in the ratio of the square root of the dimensionless powers ( $P=10$  and  $P=20$ ). The two profiles are at  $3\tau_L$  and  $6\tau_L$  after the  $P_{\text{aux}}$  is turned on.

Recent experiments in the JET (Ref. 43) with lower hybrid heating and current drive produce reversed shear discharges with reduced power thresholds for the formation of a transport barrier. Thus, as indicated by formulas (42) and (45) there is still a range of values for the threshold power depending on the magnetic shear configuration, deposition radius, and other parameters. We are in the process of making more discharge-specific simulations with detailed transport models to test the predictive power of these simulations.<sup>44</sup>

## ACKNOWLEDGMENT

This work was supported by the U.S. Department of Energy Contract No. DE-FG03-96ER-54346.

- <sup>1</sup>Y. Koide, M. Kikuchi, M. Mori *et al.*, Phys. Rev. Lett. **72**, 3662 (1994).
- <sup>2</sup>V. Parail, Y. Baranov, C. Challis *et al.*, Nucl. Fusion **39**, 429 (1999).
- <sup>3</sup>E. Mazzucato, S. Batha, M. Beer *et al.*, Phys. Rev. Lett. **77**, 3145 (1996).
- <sup>4</sup>S. Ishida, T. Fujita, H. Akasaka *et al.*, Phys. Rev. Lett. **79**, 3917 (1997).
- <sup>5</sup>H. Sugama, M. Wakatani, and A. Hasegawa, Phys. Fluids **31**, 1601 (1988).
- <sup>6</sup>B. A. Carreras, D. Newman, P. H. Diamond, and Y. M. Liang, Phys. Plasmas **1**, 4014 (1994).
- <sup>7</sup>H. Sugama and W. Horton, Plasma Phys. Controlled Fusion **37**, 345 (1995).
- <sup>8</sup>P. H. Diamond, Y. M. Liang, B. A. Carreras, and P. W. Terry, Phys. Rev. Lett. **72**, 2565 (1994).
- <sup>9</sup>V. B. Lebedev and P. H. Diamond, Phys. Plasmas **4**, 1087 (1997).
- <sup>10</sup>D. Newman, B. Carreras, D. Lopez-Bruna, P. Diamond, and V. Lebedev, Phys. Plasmas **5**, 938 (1998).
- <sup>11</sup>G. Hu and W. Horton, Phys. Plasmas **4**, 3262 (1997).
- <sup>12</sup>S. Hamaguchi and W. Horton, Phys. Fluids B **4**, 319 (1992).
- <sup>13</sup>J. L. Thiffeault and W. Horton, Phys. Plasmas **8**, 1715 (1996).
- <sup>14</sup>T. E. Hull, W. H. Enright, and K. R. Jackson, "User's Guide for DVERK—A subroutine for nonstiff ODEs," Technical Report No. 100, University of Toronto, Department of Computer Science, University of Toronto, 1976.
- <sup>15</sup>H. Sugama and W. Horton, Phys. Plasmas **4**, 405 (1997).
- <sup>16</sup>M. Erba, V. Parail, E. Springmann, and A. Taroni, Plasma Phys. Controlled Fusion **37**, 1249 (1995).
- <sup>17</sup>M. Erba, A. Cherubini, V. Parail, E. Springmann, and A. Taroni, Plasma Phys. Controlled Fusion **39**, 261 (1997).
- <sup>18</sup>W. Horton, T. Tajima, J. Q. Dong, J. Y. Kim, and Y. Kishimoto, Plasma Phys. Controlled Fusion **39**, 83 (1997).

- <sup>19</sup>G. Furnish, W. Horton, Y. Kishimoto, M. J. LeBrun, and T. Tajima, *Phys. Plasmas* **6**, 1227 (1999).
- <sup>20</sup>Y. Kishimoto, T. Tajima, W. Horton, M. J. LeBrun, and J. Y. Kim, *Phys. Plasmas* **3**, 1289 (1996).
- <sup>21</sup>R. Sydora, V. Decyk, and J. Dawson, *Plasma Phys. Controlled Fusion* **38A**, 281 (1996).
- <sup>22</sup>X. Garbet and R. Waltz, *Phys. Plasmas* **3**, 1898 (1996).
- <sup>23</sup>P. Yushmanov, J.-Q. Dong, W. Horton, and X. Su, *Phys. Plasmas* **1**, 1583 (1994).
- <sup>24</sup>J. Q. Dong, Y. Zhang, S. Mahajan, and P. Guzdar, *Phys. Plasmas* **3**, 3065 (1996).
- <sup>25</sup>G. Bateman, A. H. Kritz, J. E. Kinsey, A. J. Redd, and J. Weiland, *Phys. Plasmas* **5**, 1793 (1998).
- <sup>26</sup>H. Ninomiya and the JT-60 Team, *Phys. Fluids B* **4**, 2070 (1992).
- <sup>27</sup>J. W. Connor, G. F. Counsell, S. K. Erents, S. J. Fielding, B. LaBombard, and K. Morel, *Nucl. Fusion* **39**, 169 (1999).
- <sup>28</sup>G. M. Hogewij, N. L. L. Cardozo, M. R. D. Baar, and A. M. Schilham, *Nucl. Fusion* **38**, 1881 (1998).
- <sup>29</sup>W. Horton, H. B. Park, J. M. Kwon, D. Strozzi, P. Morrison, and D. I. Choi, *Phys. Plasmas* **5**, 3910 (1998).
- <sup>30</sup>J.-M. Kwon, W. Horton, P. Zhu, P. Morrison, H.-B. Park, and D.-I. Choi, *Phys. Plasmas* **7**, 1169 (2000).
- <sup>31</sup>F. Hinton and G. Staebler, *Phys. Fluids B* **5**, 1281 (1993).
- <sup>32</sup>G. Staebler, F. Hinton, J. Wiley, R. Dominguez, C. Greenfield, P. Gohil, T. Kurki-Suonio, and T. Osborne, *Phys. Plasmas* **1**, 909 (1994).
- <sup>33</sup>K. C. Shaing, J. E. C. Crume, and W. Houlberg, *Phys. Rev. Lett.* **63**, 2369 (1989).
- <sup>34</sup>H. Biglari, P. H. Diamond, and P. W. Terry, *Phys. Fluids B* **2**, 1 (1990).
- <sup>35</sup>Y. Zhang and S. Mahajan, *Phys. Fluids B* **5**, 2000 (1993).
- <sup>36</sup>F. Levinton, M. Zarnstorff, S. Batha *et al.*, *Phys. Rev. Lett.* **75**, 4417 (1995).
- <sup>37</sup>H. B. Park, E. G. Heo, W. Horton, and D. I. Choi, *Phys. Plasmas* **4**, 3273 (1997).
- <sup>38</sup>Y. Kishimoto, J. Y. Kim, W. Horton, T. Tajima, M. J. LeBrun, S. A. Dettrick, J. Q. Li, and S. Shirai, *Nucl. Fusion* **40**, 667 (2000).
- <sup>39</sup>Y. Koide and the JT-60 Team, *Phys. Plasmas* **4**, 1623 (1997).
- <sup>40</sup>Y. Kishimoto, J. Y. Kim, T. Fukuda, S. Ishida, T. Fujita, T. Tajima, W. Horton, G. Furnish, and M. LeBrun, in *Plasma Physics and Controlled Nuclear Fusion Research, 1996* (International Atomic Energy Agency, Vienna, 1997), paper IAEA-CN-64/DP-10.
- <sup>41</sup>D. E. Kim, D.-I. Choi, W. Horton, P. N. Yushmanov, and V. V. Parail, *Phys. Fluids B* **2**, 547 (1990).
- <sup>42</sup>I. H. Hutchinson, R. L. Boivin, and F. Bombarda, in *Fusion Energy, Sixteenth Conference Proceedings, Montreal, Canada, 1996*, Vol. 1, pp. 155–165.
- <sup>43</sup>E. Joffrin (private communication, 1999).
- <sup>44</sup>P. Zhu, G. Bateman, A. H. Kritz, and W. Horton, *Phys. Plasmas* **7**, 2898 (2000).